ACS Catalysis

pubs.acs.org/acscatalysis

Research Article

Catalytic Mechanism of Non-Target DNA Cleavage in CRISPR-Cas9 Revealed by *Ab Initio* Molecular Dynamics

Lorenzo Casalino, Łukasz Nierzwicki, Martin Jinek, and Giulia Palermo*

Cite This: *ACS Catal.* 2020, 10, 13596−13605

Read Online

ACCESS | Metrics & More | Article Recommendations | Supporting Information

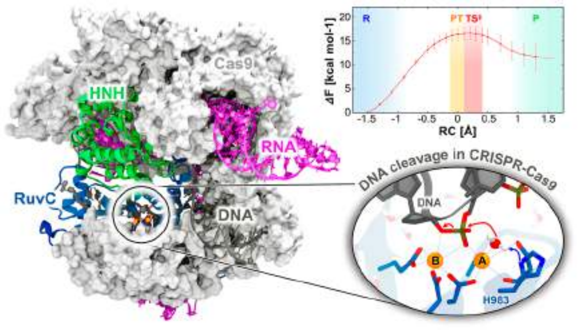

ABSTRACT: CRISPR-Cas9 is a cutting-edge genome editing technology, which uses the endonuclease Cas9 to introduce mutations at desired sites of the genome. This revolutionary tool is promising to treat a myriad of human genetic diseases. Nevertheless, the molecular basis of DNA cleavage, which is a fundamental step for genome editing, has not been established. Here, quantum−classical molecular dynamics (MD) and free energy methods are used to disclose the two-metal-dependent mechanism of phosphodiester bond cleavage in CRISPR-Cas9. *Ab initio* MD reveals a conformational rearrangement of the Mg^{2+}-bound RuvC active site, which entails the relocation of H983 to act as a general base. Then, the DNA cleavage proceeds through a concerted associative pathway fundamentally assisted by the joint dynamics of the two Mg^{2+} ions. This clarifies previous controversial experimental evidence, which could not fully establish the catalytic role of the conserved H983 and the metal cluster conformation. The comparison with other two-metal-dependent enzymes supports the identified mechanism and suggests a common catalytic strategy for genome editing and recombination. Overall, the non-target DNA cleavage catalysis described here resolves a fundamental open question in the CRISPR-Cas9 biology and provides valuable insights for improving the catalytic efficiency and the metal-dependent function of the Cas9 enzyme, which are at the basis of the development of genome editing tools.

KEYWORDS: *genome editing, QM/MM, free energy simulations, protein/nucleic acid interactions, non-coding RNA, phosphodiester bond cleavage, magnesium-aided catalysis, CRISPR-Cas9*

■ INTRODUCTION

CRISPR (clustered regularly interspaced short palindromic repeats)-Cas9 is a revolutionary genome editing tool, which is bearing innovative discoveries across the field of Life Sciences.[1] By enabling the correction of DNA mutations, this technology offers promise to treat *a priori* a myriad of human genetic diseases. Recent advances have shown the first cancer patients being infused with CRISPR-Cas9-modified T cells to increase a natural antitumor immune response.[2] The CRISPR-Cas9 "molecular scissors" use the RNA-guided endonuclease Cas9 to precisely cleave DNA sequences of interest.[3] In spite of a ground-breaking impact and widespread utilization, the catalytic mechanism of DNA cleavage, which is a fundamental step in genome editing, is not understood, potentially limiting the use of CRISPR-Cas9 for further biomedical applications. Its knowledge is paramount for improving the catalytic efficiency of the Cas9 enzyme and, in turn, for the development of novel and more specific Cas9-based genome editing tools.

Similarly to several other nuclease enzymes, Cas9 is a metal-dependent nuclease that performs Mg^{2+}-aided DNA cleavages and is inhibited by Ca^{2+}.[3,4] In the activated form of the enzymatic complex, the DNA binds Cas9 by matching a guide RNA with one strand (the target strand), while the other non-target strand is displaced and accommodated within the catalytic RuvC domain. The latter shares the structural fold of the RNA Ribonuclease H (RNase H) and is likewise thought to perform phosphodiester bond cleavages through a two-metal-ion mechanism (Figure 1A).[4,5] Nevertheless, the mechanism of DNA cleavage operated by RuvC remains nebulous and appears controversial from the available structural and biophysical studies. Structures of CRISPR-Cas9 have shown that the RuvC active site hosts three carboxylates (D10, D986, and E762),[4,6−8] which constitute the highly conserved DDE (or DEDD) motif, a fingerprint of the two-metal-dependent nucleases (Figure 1B).[9] The metal-bound X-ray structure obtained in the presence of Mn^{2+} ions revealed that the DDE motif coordinates the two catalytic metals,[3,6] while the H983 residue also approaches the active

Received: August 14, 2020
Revised: October 14, 2020

https://dx.doi.org/10.1021/acscatal.0c03566
ACS Catal. 2020, 10, 13596−13605

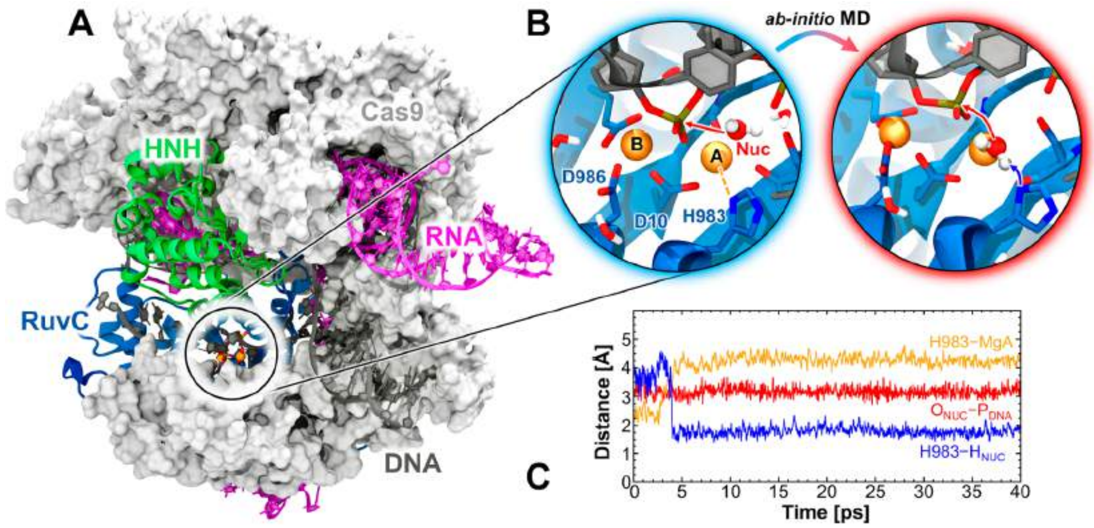

Figure 1. Overview of the CRISPR-Cas9 complex bound to a guide RNA and to a target DNA. (A) Cas9 protein is shown in the molecular surface, highlighting the HNH (green) and RuvC (blue) domains. The RNA (violet) and the DNA (black) strands are shown as ribbons. (B) Inset of the RuvC active site, displaying the catalytic metals (A and B, orange), the surrounding protein residues, and water molecules (left panel). The configuration of the active site resulting from *ab initio* molecular dynamics (MD) is shown in the right panel. The water nucleophile locates in between H983 and the scissile phosphate, positioning for the chemical reaction. (C) Time evolution along ~40 ps of *ab initio* MD of the interaction network established by H983 and by the water nucleophile. The complete set of interactions established by the metal cluster is reported in Figures S3 and S4.

site coordinating the A-site metal (MeA) with the nitrogen ligand. Previous computational studies employing extensive classical molecular dynamics (MD)[10−12] conveyed the observation that one water molecule stably coordinates MgA, in close proximity to the scissile phosphate and suitable to act as a possible nucleophile (Figure 1B, Movie S1). In this scenario, critical open questions remain unmet. First, it is unknown how the catalytically relevant Mg^{2+} ions, rather than the crystallographic Mn^{2+}, would rearrange within the active site to accomplish the catalysis. Moreover, the intricate features of the chemical mechanism, including the origin of the nucleophile initiating the chemical step and the type of catalysis leading to phosphodiester bond cleavage, have not been described. Although biochemical experiments have suggested that H983 could have a role in this chemical step,[7] crystallographic data trapping H983 in the coordination sphere of MeA arise debates on how this residue could engage in the catalysis. The efficiency and specificity of the enzyme depend on the clarification of these and on other unresolved mechanistic aspects, such as the dynamical pathway leading from the reactants (**R**) to the products (**P**), the exact mechanism for transition state (**$TS^{\ddagger}$**) stabilization, and the pivotal role and dynamics of the catalytic metals.[5,13,14] Their understanding is crucial to improve the enzyme specificity and reduce off-target cleavages, a key goal of biomedical applications of CRISPR-Cas9 genome editing.[15] Molecular simulations have contributed to understanding the biophysical function of CRISPR-Cas9.[10,12,16] By using classical and enhanced simulation methods, we previously aided the clarification of the conformational activation,[10,17,18] the selectivity,[19,20] and the allosteric function[21−23] of this genome editing tool.

Here, we establish the mechanism of phosphodiester bond cleavage within the RuvC active site through high-level quantum−classical QM(Car−Parrinello)/MM MD simulations (*ab initio* MD)[24] and free energy methods. Extensive *ab initio* MD has been carried out over multiple replicas and independent runs, reaching sub-ns collective sampling. The simulations reveal a conformational change of the RuvC active site upon substitution of the crystallographic Mn^{2+} ions with the catalytically relevant Mg^{2+}, which results in the loss of the H983 ligand by the A-site ion (MgA) and in the formation of a stable catalytic site, prone for the in-line nucleophilic attack. Then, the two-metal-dependent catalytic mechanism proceeds through a concerted (S_N2-like) associative pathway, activated by the conserved H983 and fundamentally assisted by the joint dynamics of the catalytic Mg^{2+} ions. Interestingly, a second set of *ab initio* simulations retaining the crystallographic configuration reveals an alternative phosphate-mediated cleavage, which proceeds through a concerted dissociative pathway and is unfavorable. Mutagenesis experiments showing that the H983A mutation abolishes the RuvC catalysis[7] support the active role of H983 and advocate for the H983-activated mechanism revealed here. Notably, the dynamics of the catalytic metals remarkably differs in the two chemical pathways and can be considered as a feature distinguishing the nature of phosphodiester bond cleavage in the two-metal-ion enzymes. Comparison with the two-metal-dependent enzymes further supports the identified mechanism and also suggests a common catalytic strategy for genome editing and recombination. Overall, the findings and chemical details of DNA cleavage proposed in this work provide foundational knowledge on how the endonuclease Cas9 cleaves nucleic acids and pose the basis for future investigations aimed at completing the understanding of the CRISPR-Cas9 mechanism of action. This work also represents a valuable contribution for future mechanism-based design of improved CRISPR-Cas9 genome editing tools.

■ RESULTS

Conformation of the Reactant (R). Quantum mechanical/molecular mechanical (QM/MM) MD simulations have been based on the most complete X-ray structure of CRISPR-Cas9 (PDB ID: 5F9R).[6] The active site has been treated at the

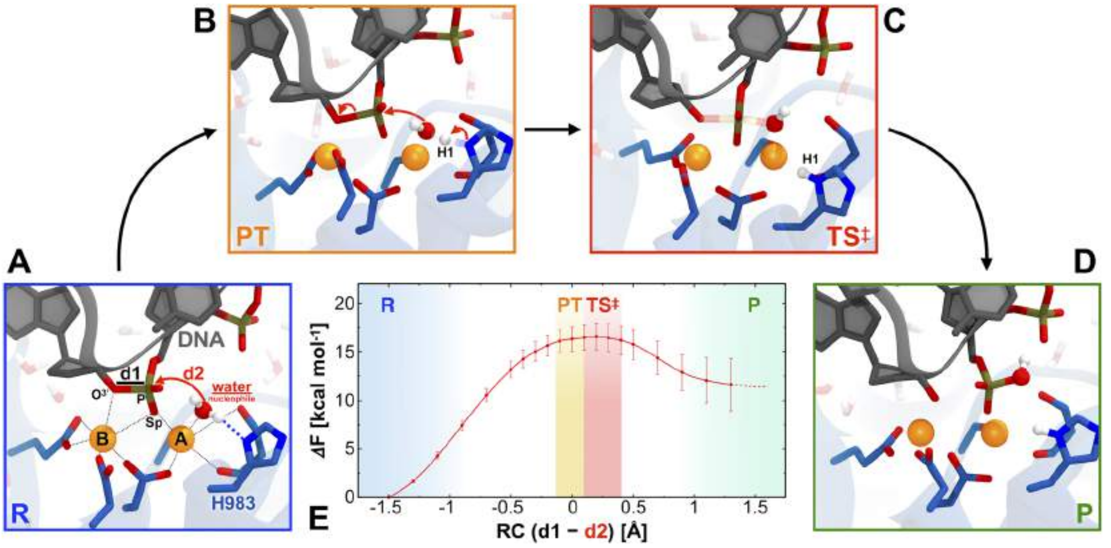

Figure 2. Structural and energetic properties of the two Mg^{2+}-aided catalysis in CRISPR-Cas9. (A) Representative snapshots of the reactant (**R**), (B) proton transfer (**PT**), (C) transition state (**TS**‡), and (D) product (**P**) states along phosphodiester bond cleavage. (E) Free energy profile ($\Delta F\#$, in kcal mol^{-1}) has been computed by using the difference in distance between the breaking ($O3'_{DNA}-P_{DNA}$, $d1$) and forming ($O_{WAT}-P_{DNA}$, $d2$) P−O bonds as a reaction coordinate (RC = $d1 - d2$, highlighted in panel A. The RC windows corresponding to the R, PT, TS‡, and P states are highlighted using colored bars.

DFT-BLYP[25,26] level of theory, while the surrounding molecular environment has been described by MM force fields, resulting into a box of ∼340 000 atoms. The QM part (105 atoms) includes the scissile and adjacent DNA phosphates groups, the two metal ions, and their coordination sphere, composed by the DDE motif and H983 (protonated in ε, as arising from previous investigations).[4,11,12] Six solvation waters have also been treated at the QM-BLYP level of theory (details are reported in the Supporting Information (SI)). The choice of simulating an enlarged QM part—including six solvation waters and protein residues, as well as the adjacent DNA phosphate groups—enabled to assess whether these chemical groups engage in the catalysis and the related proton transfer events. This is a key point because the activation of the nucleophile could occur in different ways, such as through an amino acid[27,28] or a phosphate group[29−32] serving as a general base or even through the bulk water.[33,34] Notably, these *ab initio* simulations have been performed by substituting the crystallized Mn^{2+} ions with the catalytically active Mg^{2+} ions.[4]

The investigation of the reactant (**R**) state has been initially performed through unconstrained *ab initio* MD (two replicas of ∼40 ps) in order to assess its stability and ensure that the chemical requirements for a two-metal-ion catalysis were satisfied. As a result, we observe a conformational rearrangement of the catalytic site, whereby H983 detaches from MgA while the nucleophilic water molecule simultaneously moves in between H983 and the scissile phosphate (Figure 1B). This change of the interaction network established by H983 and by the water nucleophile (Figure 2C) is observed in both simulation replicas (Figure S3). However, during these events, the water nucleophile preserves the contact with MgA, whose coordination sphere is saturated by the side-chain oxygen of S15 (Figure S3). In the final configuration, the DDE motif steadily coordinates the Mg^{2+} ions, while the scissile phosphate locates in between the two metal ions, which are jointly coordinated by the pro-*Sp* oxygen. This is a key condition for the catalysis, as it allows for the scissile phosphate to assume a configuration prone for an in-line nucleophilic attack.[5,35]

Noteworthy, a similar structural organization of the catalytic site has been also observed in a previous study performed by us as a result of ∼2.4 μs of force field-based accelerated MD followed by ∼40 ps of *ab initio* MD (Figure S4).[11] Moreover, the detachment of the H983 ligand from MgA has also been reported in some classical MD simulations, including ours,[10,12] which however do not allow for conclusive remarks on the catalysis and on the metal ions geometry, given the well-known limitations of the employed classical force-field models.[36] Interestingly, Mg^{2+} poorly binds to nitrogen, whereas Mn^{2+} shows high affinity.[37−39] In fact, it has been suggested that Mn^{2+} can contact nitrogen atoms in crystallization buffers.[39] Although one cannot generalize,[39,40] this supports the loss of the Mg^{2+}−N coordination patterns observed during classical and *ab initio* MD. To cross-validate this observation within the RuvC site, we performed unconstrained *ab initio* MD also in the presence of the crystallographic Mn^{2+} ions. As a result, MnA preserves the nitrogen ligand and the crystallographic coordination sphere over ∼40 ps (Figure S5). Taken together, these findings suggest that the coordination of MgA by means of H983 is unlikely in the RuvC site. Yet, H983 interacts with the attacking water, which in turn is stably positioned in proximity to the scissile phosphate and coordinates MgA (Figure 1B). The resulting stable configuration of the metal cluster and of the surrounding protein residues in the reactant state (**R**) laid the foundation for the investigation of the catalytic mechanism.

Mechanism of Phosphodiester Bond Cleavage. To probe the catalytic mechanism of phosphodiester bond cleavage, we performed QM/MM MD simulations in combination with free energy methods. Specifically, we employed the "blue moon ensemble" method, along with thermodynamic integration.[24] In this approach, the reaction mechanism is investigated along a selected and appropriate reaction coordinate (RC). This is progressively evolved from the **R** to the **P** through a series of sequential steps, wherein its value is kept fixed. By integrating the average (converged) constraint forces obtained along the pathway, we derived the

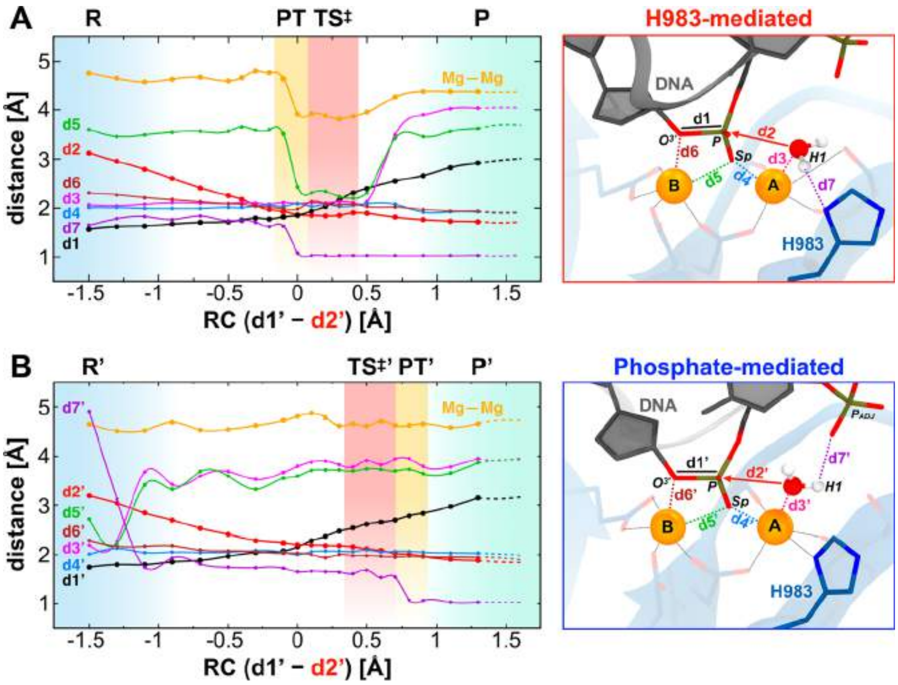

Figure 3. Interaction distances along phosphodiester bond cleavage. (A) Variation of the significant interaction distances (i.e., the Mg−Mg and the *d*1−*d*7 distances, shown on the right panel), computed at each step of the reaction coordinate (RC) in the associative reaction pathway activated by H983 (described in Figure 2). (B) Variation of the critical interaction distances along the alternative dissociative reaction pathway (described in Figure 4). The RC windows corresponding to the reactant (**R**), proton transfer (**PT**), transition state (**TS**‡), and product (**P**) states are highlighted using colored bars. The RC (i.e., difference in distance between the breaking and forming P−O bonds) and the interaction distances are described on the **R** in the right panels.

associated free energy profile (details are reported in the SI). In the present study, we used as a RC the difference in distance between the breaking (O3′$_{DNA}$−P$_{DNA}$) and forming (O$_{WAT}$−P$_{DNA}$) bonds (Figure 2A). The appropriateness of this RC for the study of phosphodiester bond cleavage has been shown in several studies of RNA/DNA processing enzymes[29,30,33,41] and is discussed in the SI. Overall, this method has been widely employed to investigate biochemical reactions,[24] including the two-metal-ion mechanism in several enzymes,[13] such as the prototypical RNase H,[29,30] and non-coding RNAs like group II intron ribozyme[33] and the spliceosome.[42] This enables a direct comparison with the current investigations of the catalytic mechanism in CRISPR-Cas9.

The simulations show that the system evolves from the reactants (**R**) to the products (**P**), separated by a transition state (**TS**‡) maximum (Figure 2 and Figure S6). The reaction is activated by H983, which acts as a general base, and proceeds through a concerted (S$_N$2-like) associative mechanism (Movie S2).[43,44] In detail, at a RC = 0 Å, a proton transfer (**PT**) event is observed, where H983 activates the nucleophilic water into a hydroxide ion by abstracting a proton right before the **TS**‡. Indeed, from RC = 0 Å (corresponding to the **PT**) to RC = 0.2 Å (highest peak of the free energy profile, corresponding to the **TS**‡), the free energy profile displays a plateau, indicating that the barrier for the proton abstraction by H983 is negligible (i.e., free energy barrier for **PT** of less than 1 kcal mol^{-1}) with respect to the **TS**‡ (details are reported in the SI). In support of this observation, a similar histidine-activated mechanism and similar energetics have been recently observed in the catalysis of the HIV-1 RNase H.[28] Upon activation, OH$^-$ becomes fully aligned with the scissile P−O3′ bond, resulting in the formation of **TS**‡. At RC = 0.4 Å, the reaction evolves downhill toward **P** formation. The associative phosphodiester bond cleavage proceeds with an overall Helmholtz free energy ($\Delta F\#$) of ~16.55 ± 1.22 kcal mol^{-1} (the convergence of the free energy profile is shown in Figure S7). The backward free energy profile (i.e., obtained by sampling along the RC in the opposite direction) was also computed, revealing no large hysteresis between the forward and backward processes (Figure S6A). The calculated activation barrier of ~16.55 ± 1.22 kcal mol^{-1} is in agreement with the experimental catalytic rate of 3.5 s^{-1} (corresponding to $\Delta G\# \sim 16/17$ kcal mol^{-1}).[45] This rate constant has been measured by distinguishing the catalysis from nucleic acid binding and providing a measure for the RuvC domain, enabling proper comparison with our computations. Importantly, biochemical experiments performed in a previous study showed that the H983A mutation abolishes the RuvC activity, therefore supporting the active role of H983 in the catalysis.[7] A full description and cross-validation of this mechanism, including the calculation of the **PT** mechanism, is given in the SI (Figure S8).

The variation of the significant interaction distances along the investigated reaction step (Figure 3A) provides insights into the role of the catalytic metals. During multiple picoseconds dynamics of the **R** state and following windows, the Mg−Mg distance remains stable around ~4.9 Å. At the **TS**‡, the two Mg^{2+} ions move closer to each other, displaying a ~1 Å shorter separation distance. At this point, the pro-*Sp* (O$_{Sp}$) oxygen approaches MgB (i.e., *d*5 in Figure 3A decreases). This is consistent with the two-metal-ion catalysis,[5,13] where the two metal ions get closer and cooperatively coordinate the reactant groups (i.e., leaving group, nucleophile and electrophile) to stabilize the **TS**‡.

During the evolution from the **R** to the **TS**‡, MgA establishes a close contact with the water's oxygen (as shown by constant values of *d*3). In this way, MgA acts as a Lewis acid, properly orienting and activating the nucleophile. Subsequently (from the **TS**‡ to the **P**), MgA detaches from the OH$^-$ group (i.e., *d*3 increases). Simultaneously, the pro-*Sp* (O_{Sp}) oxygen detaches from MgB (i.e., *d*5 increases), while MgB stably interacts with O3′ (i.e., *d*6 slightly decreases), facilitating its exit as a leaving group. Finally, starting from a RC = 0.4 Å, when the reaction evolves toward **P** formation, the Mg–Mg distance increases, as a sign that the Mg^{2+} ions move apart to facilitate the **P** release.

Alternative Reaction Pathways. To examine possible alternative reaction pathways that could take place within the RuvC active site, we performed a second set of QM/MM MD simulations always starting from the same crystal structure (PDB ID: 5F9R).[6] This time, with the aim of preserving the original crystallographic active site conformation, the initial ~40 ps long equilibration was performed, keeping the distance between H983 and MgA constrained to the crystallographic value (details in the SI). As a result of the *ab initio* MD equilibration, the water molecule does not directly interact with H983, but it forms a hydrogen bond with the adjacent phosphate (Figure 4 and Figure S6). The obtained reactant was then subjected to QM/MM free energy simulations following the same protocol adopted in the H983-activated chemical mechanism and using the same RC (details are reported in the SI). Interestingly, the catalysis proceeds though a concerted (S_N2-like), phosphate-mediated pathway (Figure 4).[43,44] Peculiarly, this mechanism shows a dissociative **TS**$^{‡\prime}$ at RC = 0.5 Å, where the breaking of the P_{DNA}–O3′ bond is more advanced than the formation of the O_{WAT}–P_{DNA} bond (Figure 3B). Immediately after the **TS**$^{‡\prime}$, the water nucleophile spontaneously releases its proton to the adjacent phosphate (Figure 3A, **PT**′), leading the chemical step to completion. A full description and cross-validation, including the **PT** mechanism, are reported in the SI (Figure S9). The overall computed Helmholtz free energy reaches a Δ*F*# value of ~18.55 ± 1.26 kcal/mol, including no large hysteresis (Figures S6B and S7). This pathway appears to be energetically unfavorable when compared to the H983-activated pathway (Figure 4). However, the difference in energy (~2 kcal mol^{-1}) lies within the statistical error of the simulations, thus suggesting that both mechanisms are theoretically possible.

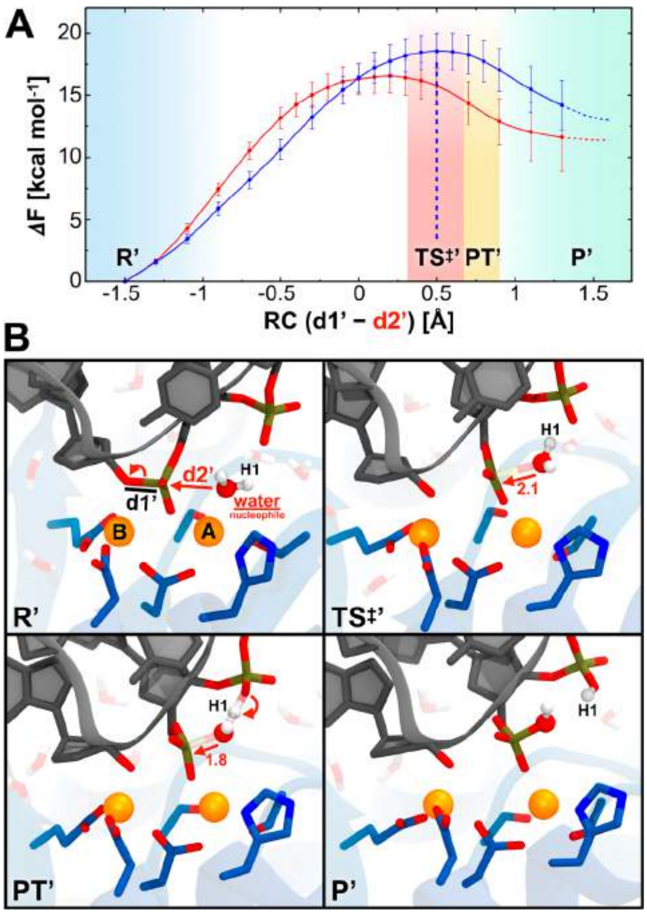

Figure 4. Alternative phosphate-mediated reaction pathway. (A) Free energy profile (Δ*F*#, in kcal mol^{-1}) for the phosphate-mediated dissociative mechanism (blue line), highlighting regions corresponding to the reactant (**R**′), transition state (**TS**$^{‡\prime}$), proton transfer (**PT**′), and products (**P**′). The free energy profile for the associative pathway activated by H983 is also shown (red line). (B) Snapshots of the **R**′, **TS**$^{‡\prime}$, **PT**′, and **P**′ states, as from the dissociative pathway.

In light of the in-depth description of phosphoryl transfer reactions previously reported,[43,44] our H983-mediated mechanism displays a concerted (S_N2-like) associative pathway, with a similar extent of partial bond formation to the nucleophile and partial bond cleavage to the leaving group at the transition state (**TS**‡, Figures 2 and 3A). The phosphate-mediated pathway displays instead a shifted **TS**‡, with slightly more bond cleavage to the leaving group than bond formation to the nucleophile (Figures 3B and 4). This was defined as a concerted (S_N2-like) dissociative pathway.[43] By inspecting the variation of the significant interaction distances along the phosphate-mediated pathway (Figure 3B), we note that, differently from the H983-mediated path (Figure 3A), MgA loosely binds the attacking water, as a sign that it does not act as a Lewis acid. Intriguingly, the distance between MgA and the water nucleophile (*d*3′ in Figure 3B) shows a similar trend to the distance between the pro-*Sp* oxygen and MgB (*d*5′). This indicates that, when the pro-*Sp* oxygen of the scissile phosphate loses coordination to MgB and fully moves onto MgA, the water nucleophile concertedly moves away from MgA. These evidences suggest that, in the dissociative mechanism, the Mg^{2+} cluster activates the electrophile (i.e., the scissile phosphate) rather than the nucleophile. A similar synchronized dynamics of the MgA–O_{WAT} and MgB–$O_{pro\text{-}Sp}$ coordination distances has also been observed in a group II intron ribozyme,[33] which displayed an analogous concerted dissociative pathway. Therefore, this suggests that this dynamical pattern of the metal cluster, and of MgA in particular, might be a hallmark of the concerted (S_N2-like) dissociative cleavage of phosphodiester bonds. On the contrary, analogously to the associative catalysis, MgB stabilizes the oxyanion leaving group. Our simulations show that throughout the entire chemical step (i.e., from **R**′ to **P**′) MgB remains in close contact with O3′, with the *d*6′ distance displaying a slight decrease toward products formation. Overall, in agreement with previous findings,[5,13,33] the observed differences in the dynamics of the catalytic metals can be seen as a signature of phosphoryl transfer events in the two-metal-ion enzymes, facilitating the interpretation of their chemical nature.

DISCUSSION

The mechanism of phosphodiester bond cleavage has been studied in several two-metal-ion enzymes,[13,27−31,34] enabling comparison with the current investigations. These studies conveyed on the associative nature of the chemical step, which requires the activation of the nucleophile, before the leaving group is dissociated. Differences in the activation of the nucleophile—i.e., whether mediated by a phosphate group,[29−32] an amino acid,[27,28] or the bulk water[34] as a general base—have been shown to be crucial for accomplishing the specific enzymatic function and for the mechanism-based design of artificial enzymes and/or selective inhibitors.[46] These previous studies support our finding of a concerted (S_N2-like) associative mechanism of DNA cleavage in CRISPR-Cas9, proceeding upon activation by H983 general base and fundamentally assisted by the joint dynamics of the two catalytic Mg^{2+} ions (Figure 2). A recent study of the HIV-1 RNase H,[28] employing a finite-temperature string method and the B3LYP functional,[26,47] disclosed a reaction mechanism similar to that of our H983-activated catalysis, with comparable energetics. In that study, a thermally accessible (i.e., with a **PT** free energy barrier less than ∼1 kcal mol^{-1} and a plateau in the free energy profile of the hydrolysis) proton abstraction by an active site histidine occurs right before a $\mathbf{TS}^{\ddagger}$ exhibiting the same extent of bond cleavage to the leaving group and bond formation to the nucleophile, analogously to the H983-mediated mechanism described here (Figure 2). A similar associative two-metal-ion mechanism involving an active site histidine has also been found in the DNA polymerase III with exonuclease activity.[27] Taken together, these studies support an associative catalysis of DNA cleavage activated by H983 (a full discussion is reported in the SI).

Our *ab initio* investigations also revealed an alternative phosphate-mediated cleavage, which proceeds through a concerted dissociative pathway energetically unfavorable than the H983-activated catalysis (Figure 4). Notably, mutagenesis and DNA cleavage experiments have probed that the H983A substitution abolishes the RuvC catalysis in CRISPR-Cas9,[7] supporting the active role of H983 evinced in our H983-activated catalytic mechanism (Figure 2). Moreover, a dissociative pathway has been rarely observed in the two-metal-dependent enzymes as either aided by Zn^{2+},[48] promoted by a non-Mg^{2+}-coordinated water,[49,50] or assisted by a single Mg^{2+} ion as recently suggested for GTP hydrolysis.[51] A similar pathway has also been reported in a group II intron ribozyme,[33] where a solvent-mediated mechanism has been proposed. However, nucleolytic ribozymes commonly react through an associative catalysis, activated by guanine nucleobases.[35,52−54] These previous studies indicate that the dissociative catalysis is rare in the two-Mg^{2+}-dependent enzymes, suggesting that the alternative phosphate-mediated dissociative mechanism proposed here could be less likely for the RuvC catalysis in CRISPR-Cas9. Notably, RuvC active site resembles that of RuvC resolvase,[55] which processes Holliday junctions during genetic recombination and postreplication repair. In this enzyme, Mg^{2+}-coordinating ligands strongly match the DDE motif in Cas9 (i.e., D7, E70, and D146 correspond to the Cas9 residues D10, E762, and D986), while the catalytic H143 locates in the position of H983 in Cas9 (Figure S10). This hints to a similar histidine-activated mechanism, advocating for a common catalytic strategy for genome editing and recombination. Remarkably, a conserved histidine flanking the DDE motif composes the active site of other Cas9 species,[8] most likely implying a similar two-metal-dependent mechanism. It is also important to mention that we cannot exclude that a third metal could engage in the RuvC catalysis, as suggested for RNA hydrolysis.[56] However, the lack of biochemical and structural data currently hampers the investigation of this hypothesis in CRISPR-Cas9. Finally, it is interesting to note that both chemical pathways identified in this study (Figures 2 and 4) display an endothermic nature, in which, according to the Hammond's postulate, the $\mathbf{TS}^{\ddagger}$ more closely resembles the products. Hence, the protonation of the O3′ could have an important contribution to the overall drive of the reaction. Considering that the pK_a of phosphomonoester groups is ∼7,[57] while that of an alkoxide is ∼16,[58] it is reasonable to expect that the proton transfer to the O3′ would lead to a gain in free energy of ∼12−13 kcal mol^{-1} (accordingly to the general relation $\Delta G = -RT \ln K$). Moreover, in CRISPR-Cas9, upon initial phosphodiester bond cleavage, RuvC can further process the DNA strand, due to not yet clearly characterized conformational changes within the active site.[59] This suggests that the postcleavage events could further contribute to the stabilization of the product. This grants future investigations employing both classical and quantum mechanical approaches to better portray the postcleavage events.

Overall, our *ab initio* approach characterizes the two-metal-ion mechanism of non-target DNA cleavage in the RuvC active site of CRISPR-Cas9, as mediated by the catalytically relevant Mg^{2+}, in agreement with experimental data.

CONCLUSIONS

Here, quantum−classical MD and free energy methods have been used to establish the two-metal-dependent mechanism of DNA cleavage in CRISPR-Cas9. *Ab initio* MD simulations, reveal that the cleavage of the DNA non-target strand occurs through a concerted associative mechanism, activated by the conserved H983 and fundamentally assisted by the joint dynamics of the two catalytic Mg^{2+} ions. The catalysis is achieved upon a critical conformational rearrangement within the RuvC active site, which occurs in the presence of the catalytically active Mg^{2+} ions and leads H983 to properly position to act as a general base. This finding resolves prior structural and biophysical controversial evidence that could not ultimately clarify the catalytic role of the conserved H983 and the metal cluster configuration.[3,6,7] The comparison with other two-metal-dependent enzymes further supports the identified mechanism and suggests a common catalytic strategy for genome editing and recombination. By carrying out a second set of *ab initio* simulations retaining the crystallographic configuration, we further characterized an alternative phosphate-mediated cleavage, which appears energetically slightly unfavorable. Notably, experimental evidences depict H983 as an essential active element for retention of catalysis in CRISPR-Cas9.[7] This strongly advocates for the H983-activated mechanism observed here upon the conformational change of the RuvC active site. Intriguingly, the joint dynamics and the role of the metal ions are shown to remarkably differ in the in the two chemical pathways, revealing a hallmark of the enzymatic two-metal-ion mechanism. Overall, this work addresses a fundamental open question in the CRISPR-Cas9 biology, which has remained unclear from previous experimental studies. The chemical aspects and the mechanistic details of the DNA cleavage provided here are critical for understanding the catalytic function of CRISPR-Cas9, which is at the basis of its use as a genome editing tool. This knowledge lays the foundation for improving the catalytic efficiency and the specificity of CRISPR-Cas9, paving the way for future therapeutic applications of this gene editing technology.

■ MATERIALS AND METHODS

Structural Models. Molecular simulations have been carried out on the activated form of the *Streptococcus pyogenes* CRISPR-Cas9 enzymatic complex, which has been based on the most complete X-ray structure of Cas9 in complex with RNA and DNA (PDB: 5F9R).[6] This model system has been embedded in explicit waters, and counterions have been added to neutralize the total charge, leading to a periodic simulations cell of ∼180 × 120 × 140 Å^3 and a total of ∼340 000 atoms. Full details are reported in the SI.

Classical Molecular Dynamics (MD). Classical MD has been performed to equilibrate the system prior to *ab initio* MD, using the Amber ff12SB force field, which includes the ff99bsc0 corrections for DNA[60] and the ff99bsc0+$\chi OL3$ corrections for RNA.[61,62] The TIP3P model was employed for water molecules,[63] while the Åqvist force field was used for Mg^{2+} ions.[64] An integration time step of 2 fs was used. Hydrogen atoms were added assuming standard bond lengths and were constrained to their equilibrium position with the SHAKE algorithm. A temperature control (300 K) was performed *via* Langevin dynamics,[65] with a collision frequency $\gamma = 1$. Pressure control was accomplished by coupling the system to a Berendsen barostat,[66] at a reference pressure of 1 atm and with a relaxation time of 2 ps. The simulations were carried out with the following protocol. The system was subjected to energy minimization to relax the water molecules and the counterions, keeping the protein, as well as the RNA, DNA, and Mg^{2+} ions fixed with harmonic position restraints of 300 kcal/mol·Å^2. Then, the system was heated from 0 to 100 K in the canonical ensemble (NVT), by running two NVT simulations of 5 ps each, imposing position restraints of 100 kcal/mol · Å^2 on the above-mentioned elements of the system. The temperature was further increased up to 200 K in ∼100 ps of MD in the isothermal−isobaric ensemble (NPT), in which the restraint was reduced to 25 kcal/mol·Å^2. Subsequently, all restraints were released and the temperature was raised up to 300 K in a single NPT simulation of 500 ps. After ∼1.1 ns of equilibration, ∼10 ns of NPT production was carried out allowing for the density of the system to stabilize around 1.01 g/cm^{-3}. The obtained systemwas used as a starting point for QM/MM simulations. Classical MD was performed with the GPU version of AMBER 18.[67]

***Ab Initio* Quantum Mechanics/Molecular Mechanics (QM/MM) Simulations.** In the QM/MM simulations, the RuvC active site was treated at a QM level of theory, while the rest of the system (including explicit waters) has been described using the classical force field. The QM part included the catalytic Mg^{2+} ions and their coordinating protein residues E762, D986, D10, S15, I11, and H983 (protonated in ε, as shown by a number of previous studies),[4,11,12] part of the DNA nucleobases C-3 and A-4 and six water molecules (Figure S1). This resulted in a total of 105 QM atoms and an additional 13 capping hydrogen atoms used to saturate the valence of the terminal QM atoms. The QM atoms were described at the QM DFT/BLYP[25,26] level, while the remaining MM part was treated using the force field described above. QM/MM simulations were performed using the CPMD code (www.cpmd.org). The wave functions were expanded in a plane wave basis setup to a cutoff of 75 Ry in a QM cell of dimensions ∼26 × 22 × 26 Å^3. The interactions between the valence electrons and ionic cores were described with norm-conserving Martins-Troullier pseudopotentials.[68] The QM part was treated as an isolated system, and electrostatic interactions between periodic images were decoupled by the scheme of Tuckerman.[69] A rigorous Hamiltonian treatment of the electrostatic interaction between the QM and MM regions was used.[70] The QM/MM protocol consisted of an initial optimization of the wave function, followed by ∼6 ps of careful equilibration carried out with Born−Oppenheimer (BO) MD in the canonical (NVT) ensemble using an integration time step of 20 au (∼0.48 fs). The temperatures of the QM and MM subsystems were kept constant at 300 K using a Nosé−Hoover thermostat.[71,72] After this initial phase, Car−Parrinello (CP) QM/MM simulations[73] were carried out with a time step of 5 au (∼0.12 fs) and a fictitious electron mass of 600 au. These unconstrained *ab initio* simulations were carried out reaching ∼40 ps of sampling in two replicas, initialized from different coordinates and velocities. The final configuration was simulated for other ∼40 ps of unconstrained *ab initio* MD. An additional ∼40 ps of *ab initio* MD was also carried out in the presence of the crystallized Mn^{2+} ions.[4] Full details are reported in the SI.

Free Energy Simulations. The free energy profiles associated with phosphodiester bond cleavage were obtained through QM/MM simulations and free energy methods. The "blue moon ensemble" method,[74] along with thermodynamic integration, were employed to investigate phosphodiester bond cleavage, using the difference in distance between the breaking ($O3'_{DNA}-P_{DNA}$) and forming ($O_{WAT}-P_{DNA}$) bonds as a reaction coordinate (RC). The appropriateness of this approach and of the employed RC have been shown in several studies of DNA/RNA processing enzymes,[28−30,33] and are further discussed in the SI. Starting from a value of the RC = −1.5 Å (i.e., the reactant **R** state), we sampled in 20 sequential windows along the RC, with a resolution of 0.2 Å (0.1 Å in the region in the vicinity of the **TS**‡). A growth rate of 0.1 Å/ps was used to move from a window to the following one. Then, each window has been simulated for ≥6 ps, reaching convergence of the constraint force and collecting a total of *ab initio* QM/MM MD of ∼120 ps. By using this approach, we computed two free energy profiles, starting from two different configurations shown in Figure 1B (right and left panels, respectively). This resulted in a total of ∼240 ps of sampling. In order to estimate the error associated with hysteresis, we also computed the backward reaction pathways. For each free energy profile, we selected a point after the **TS**‡ was reached and we followed the backward pathway by sampling over eight consecutive windows for ≥6 ps each (a complete description is given in the SI). This reached a total sampling of an additional ∼90 ps. Notably, these calculations revealed no large hysteresis between the forward and backward pathways (Figure S6). Finally, for both free energy profiles, at a RC = 1.2 Å, the constraint was released for ∼5 ps, enabling the system to spontaneously reach the product state. The derivation of all free energy profiles (both forward and backward pathways) was performed by considering the average constraint force within each window from the points in which the force reached the convergence along the equilibrated trajectory. The statistical error at each point of the free energy profiles (both forward and backward pathways) was computed by error propagation analysis. Finally, the overall error on the free energy barrier was estimated as the sum of the statistical error and the error due to hysteresis between the forward and backward pathways (Figure S6). This resulted in a total Helmholtz's free energy of ~16.55 ± 1.22 kcal mol^{-1} for the H983-mediated free energy profile (Figure 2) and ~18.55 ± 1.26 kcal mol^{-1} for the phosphate-mediated free energy profile (Figure 4). As in previous studies based on *ab initio* MD,[24,29,42] further exploration of the identified chemical mechanism included the explicit calculation of the proton transfer in the H983-activated pathway. These simulations required an additional ~33 ps of sampling and are described in the SI. Overall, unconstrained *ab-initio* MD and free energy simulations have been carried out collecting a total of ~640 ps. Considering the high cost of *ab-initio* MD, the sampling collected here has been at the limits of our computational facility at the San Diego Supercomputing Center (SDSC). The SI comprehensively describes the application of *ab initio* MD and free energy methods.

■ ASSOCIATED CONTENT

Supporting Information

The Supporting Information is available free of charge at https://pubs.acs.org/doi/10.1021/acscatal.0c03566.

> Discussions of structural models used, classical molecular dynamics (MD) simulations, *ab initio* quantum mechanics/molecular mechanics simulations, free energy simulations, cross-validation of the free energy profiles, time evolution over classical and *ab initio* MD simulations of relevant structural and energetic properties (PDF)
>
> Movie of overview of the structural model of the CRISPR-Cas9 complex bound to a guide RNA and to a target DNA (MPG)
>
> Movie of two-metal ion mechanism of phosphodiester bond cleavage in CRISPR-Cas9, computed through QM (Car-Parrinello)/MM MD simulations (MPG)

■ AUTHOR INFORMATION

Corresponding Author

Giulia Palermo − *Department of Bioengineering and Department of Chemistry, University of California Riverside, Riverside, California 92521, United States;* orcid.org/0000-0003-1404-8737; Email: giulia.palermo@ucr.edu

Authors

Lorenzo Casalino − *Department of Chemistry and Biochemistry, University of California San Diego, La Jolla, California 92093, United States;* orcid.org/0000-0003-3581-1148

Łukasz Nierzwicki − *Department of Bioengineering, University of California Riverside, Riverside, California 92521, United States*

Martin Jinek − *Department of Biochemistry, University of Zürich, CH-8057 Zürich, Switzerland*

Complete contact information is available at: https://pubs.acs.org/10.1021/acscatal.0c03566

Notes

The authors declare no competing financial interest.

■ ACKNOWLEDGMENTS

The authors would like to thank Michele Cascella and Martin Pacesa for useful discussions. This material is based upon work supported by the National Science Foundation under Grant No. CHE-1905374. This work was also partially funded by NIH Grant R01 EY027440. Computer time was provided by the Extreme Science and Engineering Discovery Environment (XSEDE) through the grant TG-MCB160059.

■ REFERENCES

(1) Doudna, J. A.; Charpentier, E. Genome Editing. The New Frontier of Genome Engineering with CRISPR-Cas9. *Science* **2014**, *346*, 1258096.

(2) Stadtmauer, E. A.; Fraietta, J. A.; Davis, M. M.; Cohen, A. D.; Weber, K. L.; Lancaster, E.; Mangan, P. A.; Kulikovskaya, I.; Gupta, M.; Chen, F.; Tian, L.; Gonzalez, V. E.; Xu, J.; Jung, I.; Melenhorst, J. J.; Plesa, G.; Shea, J.; Matlawski, T.; Cervini, A.; Gaymon, A. L.; Desjardins, S.; Lamontagne, A.; Salas-Mckee, J.; Fesnak, A.; Siegel, D. L.; Levine, B. L.; Jadlowsky, J. K.; Young, R. M.; Chew, A.; Hwang, W.; Hexner, E. O.; Carreno, B. M.; Nobles, C. L.; Bushman, F. D.; Parker, K. R.; Qi, Y.; Satpathy, A. T.; Chang, H. Y.; Zhao, Y.; Lacey, S. F.; June, C. H. CRISPR-Engineered T Cells in Patients with Refractory Cancer. *Science* **2020**, *367*, eaba7365.

(3) Jinek, M.; Chylinski, K.; Fonfara, I.; Hauer, M.; Doudna, J. A.; Charpentier, E. A Programmable Dual-RNA-Guided DNA Endonuclease in Adaptive Bacterial Immunity. *Science* **2012**, *337*, 816−821.

(4) Jinek, M.; Jiang, F.; Taylor, D. W.; Sternberg, S. H.; Kaya, E.; Ma, E.; Anders, C.; Hauer, M.; Zhou, K.; Lin, S.; Kaplan, M.; Iavarone, A. T.; Charpentier, E.; Nogales, E.; Doudna, J. A. Structures of Cas9 Endonucleases Reveal RNA-Mediated Conformational Activation. *Science* **2014**, *343*, 1247997−1247997.

(5) Steitz, T. A.; Steitz, J. A. A General Two-Metal-Ion Mechanism for Catalytic RNA. *Proc. Natl. Acad. Sci. U. S. A.* **1993**, *90*, 6498−6502.

(6) Jiang, F.; Taylor, D. W.; Chen, J. S.; Kornfeld, J. E.; Zhou, K.; Thompson, A. J.; Nogales, E.; Doudna, J. A. Structures of a CRISPR-Cas9 R-Loop Complex Primed for DNA Cleavage. *Science* **2016**, *351*, 867−871.

(7) Nishimasu, H.; Ran, F. A.; Hsu, P. D.; Konermann, S.; Shehata, S. I.; Dohmae, N.; Ishitani, R.; Zhang, F.; Nureki, O. Crystal Structure of Cas9 in Complex with Guide RNA and Target DNA. *Cell* **2014**, *156*, 935−949.

(8) Jiang, F.; Doudna, J. A. CRISPR−Cas9 Structures and Mechanisms. *Annu. Rev. Biophys.* **2017**, *46*, 505−529.

(9) Yang, W. Nucleases: Diversity of Structure, Function and Mechanism. *Q. Rev. Biophys.* **2011**, *44*, 1−93.

(10) Palermo, G.; Miao, Y.; Walker, R. C.; Jinek, M.; McCammon, J. A. CRISPR-Cas9 Conformational Activation as Elucidated from Enhanced Molecular Simulations. *Proc. Natl. Acad. Sci. U. S. A.* **2017**, *114*, 7260−7265.

(11) Palermo, G. Structure and Dynamics of the CRISPR−Cas9 Catalytic Complex. *J. Chem. Inf. Model.* **2019**, *59*, 2394−2406.

(12) Zuo, Z.; Liu, J. Cas9-Catalyzed DNA Cleavage Generates Staggered Ends: Evidence from Molecular Dynamics Simulations. *Sci. Rep.* **2016**, *6*, 37584.

(13) Palermo, G.; Cavalli, A.; Klein, M. L.; Alfonso-Prieto, M.; Dal Peraro, M.; De Vivo, M. Catalytic Metal Ions and Enzymatic Processing of DNA and RNA. *Acc. Chem. Res.* **2015**, *48*, 220−228.

(14) Berta, D.; Buigues, P. J.; Badaoui, M.; Rosta, E. Cations in Motion: QM/MM Studies of the Dynamic and Electrostatic Roles of H^+ and Mg^{2+} Ions in Enzyme Reactions. *Curr. Opin. Struct. Biol.* **2020**, *61*, 198−206.

(15) Fu, Y.; Foden, J. A.; Khayter, C.; Maeder, M. L.; Reyon, D.; Joung, J. K.; Sander, J. D. High-Frequency off-Target Mutagenesis Induced by CRISPR-Cas Nucleases in Human Cells. *Nat. Biotechnol.* **2013**, *31*, 822−826.

(16) Ray, A.; Di Felice, R. Protein-Mutation-Induced Conformational Changes of the DNA and Nuclease Domain in CRISPR/Cas9

Systems by Molecular Dynamics Simulations. *J. Phys. Chem. B* **2020**, *124*, 2168−2179.

(17) Palermo, G.; Miao, Y.; Walker, R. C.; Jinek, M.; McCammon, J. A. Striking Plasticity of CRISPR-Cas9 and Key Role of Non-Target DNA, as Revealed by Molecular Simulations. *ACS Cent. Sci.* **2016**, *2*, 756−763.

(18) Palermo, G.; Chen, J. S.; Ricci, C. G.; Rivalta, I.; Jinek, M.; Batista, V. S.; Doudna, J. A.; McCammon, J. A. Key Role of the REC Lobe during CRISPR-Cas9 Activation by 'Sensing', 'Regulating', and 'Locking' the Catalytic HNH Domain. *Q. Rev. Biophys.* **2018**, *51*, No. e9.

(19) Ricci, C. G.; Chen, J. S.; Miao, Y.; Jinek, M.; Doudna, J. A.; McCammon, J. A.; Palermo, G. Deciphering Off-Target Effects in CRISPR-Cas9 through Accelerated Molecular Dynamics. *ACS Cent. Sci.* **2019**, *5*, 651−662.

(20) Mitchell, B. P.; Hsu, R. V.; Medrano, M. A.; Zewde, N. T.; Narkhede, Y. B.; Palermo, G. Spontaneous embedding of DNA mismatches within the RNA:DNA hybrid of CRISPR-Cas9. *Front Mol Biosci.* **2020**, *7*, 39.

(21) Nierzwicki, Ł.; Arantes, P. R.; Saha, A.; Palermo, G. Establishing the Allosteric Mecanism in CRISPR-Cas9. *Wiley Interdiscip. Rev.: Comput. Mol. Sci.* **2020**, No. e1503.

(22) Palermo, G.; Ricci, C. G.; Fernando, A.; Basak, R.; Jinek, M.; Rivalta, I.; Batista, V. S.; McCammon, J. A. Protospacer Adjacent Motif-Induced Allostery Activates CRISPR-Cas9. *J. Am. Chem. Soc.* **2017**, *139*, 16028−16031.

(23) East, K. W.; Newton, J. C.; Morzan, U. N.; Narkhede, Y. B.; Acharya, A.; Skeens, E.; Jogl, G.; Batista, V. S.; Palermo, G.; Lisi, G. P. Allosteric Motions of the CRISPR−Cas9 HNH Nuclease Probed by NMR and Molecular Dynamics. *J. Am. Chem. Soc.* **2020**, *142*, 1348−1358.

(24) Brunk, E.; Rothlisberger, U. Mixed Quantum Mechanical/Molecular Mechanical Molecular Dynamics Simulations of Biological Systems in Ground and Electronically Excited States. *Chem. Rev.* **2015**, *115*, 6217−6263.

(25) Becke, A. D. Density-Functional Exchange-Energy Approximation with Correct Asymptotic Behavior. *Phys. Rev. A: At., Mol., Opt. Phys.* **1988**, *38*, 3098−3100.

(26) Lee, C.; Yang, W.; Parr, R. G. Development of the Colle-Salvetti Correlation-Energy Formula into a Functional of the Electron Density. *Phys. Rev. B: Condens. Matter Mater. Phys.* **1988**, *37*, 785−789.

(27) Cisneros, G. A.; Perera, L.; Schaaper, R. M.; Pedersen, L. C.; London, R. E.; Pedersen, L. G.; Darden, T. A. Reaction Mechanism of the ε Subunit of *E. Coli* DNA Polymerase III: Insights into Active Site Metal Coordination and Catalytically Significant Residues. *J. Am. Chem. Soc.* **2009**, *131*, 1550−1556.

(28) Dürr, S. L.; Bohuszewicz, O.; Suardiaz, R.; Jambrina, P. G.; Peter, C.; Shao, Y.; Rosta, E. The dual role of histidine as general base and recruiter of a third metal ion in HIV-1 RNase H. *ChemRxiv preprint* **2019**, 1 DOI: 10.26434/chemrxiv.8224538.v1.

(29) De Vivo, M.; Dal Peraro, M.; Klein, M. L. Phosphodiester Cleavage in Ribonuclease H Occurs via an Associative Two-Metal-Aided Catalytic Mechanism. *J. Am. Chem. Soc.* **2008**, *130*, 10955−10962.

(30) Rosta, E.; Nowotny, M.; Yang, W.; Hummer, G. Catalytic Mechanism of RNA Backbone Cleavage by Ribonuclease H from Quantum Mechanics/Molecular Mechanics Simulations. *J. Am. Chem. Soc.* **2011**, *133*, 8934−8941.

(31) Lei, J.; Sheng, G.; Cheung, P. P.-H.; Wang, S.; Li, Y.; Gao, X.; Zhang, Y.; Wang, Y.; Huang, X. Two Symmetric Arginine Residues Play Distinct Roles in Thermus Thermophilus Argonaute DNA Guide Strand-Mediated DNA Target Cleavage. *Proc. Natl. Acad. Sci. U. S. A.* **2019**, *116*, 845−853.

(32) Tse, C. K. M.; Xu, J.; Xu, L.; Sheong, F. K.; Wang, S.; Chow, H. Y.; Gao, X.; Li, X.; Cheung, P. P. H.; Wang, D.; Zhang, Y.; Huang, X. Intrinsic Cleavage of RNA Polymerase II Adopts a Nucleobase-Independent Mechanism Assisted by Transcript Phosphate. *Nat. Catal.* **2019**, *2*, 228−235.

(33) Casalino, L.; Palermo, G.; Rothlisberger, U.; Magistrato, A. Who Activates the Nucleophile in Ribozyme Catalysis? An Answer from the Splicing Mechanism of Group II Introns. *J. Am. Chem. Soc.* **2016**, *138*, 10374−10377.

(34) Ribeiro, A. J. M.; Ramos, M. J.; Fernandes, P. A. The Catalytic Mechanism of HIV-1 Integrase for DNA 3′-End Processing Established by QM/MM Calculations. *J. Am. Chem. Soc.* **2012**, *134*, 13436−13447.

(35) Wilson, T. J.; Liu, Y.; Lilley, D. M. J. Ribozymes and the Mechanisms That Underlie RNA Catalysis. *Front. Chem. Sci. Eng.* **2016**, *10*, 178−185.

(36) Li, P.; Merz, K. M. Metal Ion Modeling Using Classical Mechanics. *Chem. Rev.* **2017**, *117*, 1564−1686.

(37) Bock, C. W.; Katz, A. K.; Markham, G. D.; Glusker, J. P. Manganese as a Replacement for Magnesium and Zinc: Functional Comparison of the Divalent Ions. *J. Am. Chem. Soc.* **1999**, *121*, 7360−7372.

(38) Wedekind, J. E.; Dutta, D.; Belashov, I. A.; Jenkins, J. L. Metalloriboswitches: RNA-Based Inorganic Ion Sensors That Regulate Genes. *J. Biol. Chem.* **2017**, *292*, 9441−9450.

(39) Leonarski, F.; D'Ascenzo, L.; Auffinger, P. Mg^{2+} Ions: Do They Bind to Nucleobase Nitrogens? *Nucleic Acids Res.* **2017**, *45*, 987−1004.

(40) Schmeing, T. M.; Huang, K. S.; Kitchen, D. E.; Strobel, S. A.; Steitz, T. A. Structural Insights into the Roles of Water and the 2′ Hydroxyl of the P Site TRNA in the Peptidyl Transferase Reaction. *Mol. Cell* **2005**, *20*, 437−448.

(41) Ivanov, I.; Tainer, J. A.; McCammon, J. A. Unraveling the Three-Metal-Ion Catalytic Mechanism of the DNA Repair Enzyme Endonuclease IV. *Proc. Natl. Acad. Sci. U. S. A.* **2007**, *104*, 1465−1470.

(42) Borišek, J.; Magistrato, A. All-Atom Simulations Decrypt the Molecular Terms of RNA Catalysis in the Exon-Ligation Step of the Spliceosome. *ACS Catal.* **2020**, *10*, 5328−5334.

(43) Kamerlin, S. C. L.; Sharma, P. K.; Prasad, R. B.; Warshel, A. Why Nature Really Chose Phosphate. *Q. Rev. Biophys.* **2013**, *46*, 1−132.

(44) Lassila, J. K.; Zalatan, J. G.; Herschlag, D. Biological Phosphoryl-Transfer Reactions: Understanding Mechanism and Catalysis. *Annu. Rev. Biochem.* **2011**, *80*, 669−702.

(45) Gong, S.; Yu, H. H.; Johnson, K. A.; Taylor, D. W. DNA Unwinding Is the Primary Determinant of CRISPR-Cas9 Activity. *Cell Rep.* **2018**, *22*, 359−371.

(46) Klumpp, K.; Hang, J. Q.; Rajendran, S.; Yang, Y.; Derosier, A.; Wong Kai In, P.; Overton, H.; Parkes, K. E. B.; Cammack, N.; Martin, J. A. Two-Metal Ion Mechanism of RNA Cleavage by HIV RNase H and Mechanism-Based Design of Selective HIV RNase H Inhibitors. *Nucleic Acids Res.* **2003**, *31*, 6852−6859.

(47) Becke, A. D. A New Mixing of Hartree−Fock and Local Density-functional Theories. *J. Chem. Phys.* **1993**, *98*, 1372−1377.

(48) Lopez-Canut, V.; Roca, M.; Bertran, J.; Moliner, V.; Tunon, I. Theoretical Study of Phosphodiester Hydrolysis in Nucleotide Pyrophosphatase/Phosphodiesterase. Environmental Effects on the Reaction Mechanism. *J. Am. Chem. Soc.* **2010**, *132*, 6955−6963.

(49) Akola, J.; Jones, R. O. Density Functional Calculations of ATP Systems. 2. ATP Hydrolysis at the Active Site of Actin. *J. Phys. Chem. B* **2006**, *110*, 8121−8129.

(50) Imhof, P.; Fischer, S.; Smith, J. C. Catalytic Mechanism of DNA Backbone Cleavage by the Restriction Enzyme EcoRV: A Quantum Mechanical/Molecular Mechanical Analysis. *Biochemistry* **2009**, *48*, 9061−9075.

(51) Calixto, A. R.; Moreira, C.; Pabis, A.; Kotting, C.; Gerwert, K.; Rudack, T.; Kamerlin, S. C.L. GTP Hydrolysis Without an Active Site Base: A Unifying Mechanism for Ras and Related GTPases. *J. Am. Chem. Soc.* **2019**, *141*, 10684−10701.

(52) Chen, H.; Giese, T. J.; Golden, B. L.; York, D. M. Divalent Metal Ion Activation of a Guanine General Base in the Hammerhead Ribozyme: Insights from Molecular Simulations. *Biochemistry* **2017**, *56*, 2985−2994.

(53) Mlýnský, V.; Walter, N. G.; Šponer, J.; Otyepka, M.; Banáš, P. The Role of an Active Site Mg^{2+} in HDV Ribozyme Self-Cleavage: Insights from QM/MM Calculations. *Phys. Chem. Chem. Phys.* **2015**, *17*, 670−679.

(54) Zhang, S.; Ganguly, A.; Goyal, P.; Bingaman, J. L.; Bevilacqua, P. C.; Hammes-Schiffer, S. Role ofthe Active Site Guanine in the GlmS Ribozyme Self-Cleavage: Quantum Mechanical/Molecular Mechanical Energy Simulations. *J. Am. Chem. Soc.* **2015**, *137*, 784−798.

(55) Górecka, K. M.; Komorowska, W.; Nowotny, M. Crystal Structure of RuvC Resolvase in Complex with Holliday Junction Substrate. *Nucleic Acids Res.* **2013**, *41*, 9945−9955.

(56) Samara, N. L.; Yang, W. Cation Trafficking Propels RNA Hydrolysis. *Nat. Struct. Mol. Biol.* **2018**, *25*, 715−721.

(57) Thaplyal, P.; Bevilacqua, P. C. Experimental Approaches for Measuring PKa's in RNA and DNA. *Methods Enzymol.* **2014**, *549*, 189−219.

(58) Feng, S.; Bagia, C.; Mpourmpakis, G. Determination of Proton Affinities and Acidity Constants of Sugars. *J. Phys. Chem. A* **2013**, *117*, 5211−5219.

(59) Stephenson, A. A.; Raper, A. T.; Suo, Z. Bidirectional Degradation of DNA Cleavage Products Catalyzed by CRISPR/Cas9. *J. Am. Chem. Soc.* **2018**, *140*, 3743−3750.

(60) Perez, A.; Marchan, I.; Svozil, D.; Sponer, J.; Cheatham, T. E., 3rd; Laughton, C. A.; Orozco, M. Refinement of the AMBER Force Field for Nucleic Acids: Improving the Description of Alpha/Gamma Conformers. *Biophys. J.* **2007**, *92*, 3817−3829.

(61) Banas, P.; Hollas, D.; Zgarbova, M.; Jurecka, P.; Orozco, M.; Cheatham, T. E., 3rd; Sponer, J.; Otyepka, M. Performance of Molecular Mechanics Force Fields for RNA Simulations: Stability of UUCG and GNRA Hairpins. *J. Chem. Theory Comput.* **2010**, *6*, 3836−3849.

(62) Zgarbova, M.; Otyepka, M.; Sponer, J.; Mladek, A.; Banas, P.; Cheatham, T. E.; Jurecka, P. Refinement of the Cornell Nucleic Acids Force Field Based on Reference Quantum Chemical Calculations of Glycosidic Torsion Profiles. *J. Chem. Theory Comput.* **2011**, *7*, 2886−2902.

(63) Jorgensen, W. L.; Chandrasekhar, J.; Madura, J. D.; Impey, R. W.; Klein, M. L. Comparison of Simple Potential Functions for Simulating Liquid Water. *J. Chem. Phys.* **1983**, *79*, 926−935.

(64) Aqvist, J. Ion-Water Interaction Potentials Derived from Free Energy Perturbation Simulations. *J. Phys. Chem.* **1990**, *94*, 8021−8024.

(65) Turq, P.; Lantelme, sF.; Friedman, H. L. Brownian Dynamics: Its Applications to Ionic Solutions. *J. Chem. Phys.* **1977**, *66*, 3039.

(66) Berendsen, H. J. C.; Postma, J. P. M.; van Gunsteren, W. F.; DiNola, A.; Haak, J. R. Molecular Dynamics with Coupling to an External Bath. *J. Chem. Phys.* **1984**, *81*, 3684.

(67) Case, D. A.; Betz, R. M.; Botello-Smith, W.; Cerutti, D. S.; Cheatham, I. T. E.; Darden, T. A.; Duke, R. E.; Giese, T. J.; Gohlke, H.; Goetz, A. W.; Homeyer, N.; Izadi, S.; Janowski, P.; Kaus, J.; Kovalenko, A.; Lee, T. S.; LeGrand, S.; Li, P.; Lin, C.; Luchko, T.; Luo, R.; Madej, B.; Mermelstein, D.; Merz, K. M.; Monard, G.; Nguyen, H.; Nguyen, H. T.; Omelyan, I.; Onufriev, A.; Roe, D. R.; Roitberg, A.; Sagui, C.; Simmerling, C. L.; Swails, J.; Walker, R. C.; Wang, J.; Wolf, R. M.; Wu, X.; Xiong, Y.; Xue, Y.; York, D. M.; Kollman, P. A. *AMBER 2018*; University of California: San Francisco, 2018.

(68) Troullier, N.; Martins, J. L. Efficient Pseudopotentials for Plane-Wave Calculations. II. Operators for Fast Iterative Diagonalization. *Phys. Rev. B: Condens. Matter Mater. Phys.* **1991**, *43*, 8861−8869.

(69) Martyna, G. J.; Tuckerman, M. E. A Reciprocal Space Based Method for Treating Long Range Interactions in Ab Initio and Force-Field-Based Calculations in Clusters. *J. Chem. Phys.* **1999**, *110*, 2810−2821.

(70) Laio, A.; VandeVondele, J.; Rothlisberger, U. A Hamiltonian Electrostatic Coupling Scheme for Hybrid Car−Parrinello Molecular Dynamics Simulations. *J. Chem. Phys.* **2002**, *116*, 6941−6947.

(71) Hoover, W. G. Canonical Dynamics: Equilibrium Phase-Space Distributions. *Phys. Rev. A: At., Mol., Opt. Phys.* **1985**, *31*, 1695−1697.

(72) Nosé, S. An Extension of the Canonical Ensemble Molecular Dynamics Method. *Mol. Phys.* **1986**, *57*, 187−191.

(73) Car, R.; Parrinello, M. Unified Approach for Molecular Dynamics and Density-Functional Theory. *Phys. Rev. Lett.* **1985**, *55*, 2471−2474.

(74) Carter, E. A.; Ciccotti, G.; Hynes, J. T.; Kapral, R. Constrained Reaction Coordinate Dynamics for the Simulation of Rare Events. *Chem. Phys. Lett.* **1989**, *156*, 472−477.